Voltage-controlled magnetic anisotropy in heterostructures with a two-dimensional magnetic material

Qilong Sun,[1,*] Miaojia Yuan,[1] Zhenkui Zhang,[2] and Nicholas Kioussis[3,†]
[1]*School of Science, Shandong Jianzhu University, Jinan, Shandong 250101, China*
[2]*School of Science, Langfang Normal University, Langfang, Hebei 065000, China*
[3]*Department of Physics and Astronomy, California State University, Northridge, California 91330, USA*

(Received 14 September 2022; accepted 8 February 2023; published 21 February 2023)

The advent of two-dimensional (2D) magnetic materials significantly expand the scope of voltage-controlled magnetization-switching scheme as their integration in diverse magnetic tunnel junctions (MTJ) offers a highly attractive perspective for designing future magnetoelectric random access memory (MeRAM). Here, we propose the utilization of 2D ferromagnetic Fe_2I_2 to substitute traditional magnetic thin films for assembling energy-efficient MTJs combined with Ir capping layers. We find these multilayers exhibit both giant perpendicular magnetic anisotropy (PMA) and voltage controlled magnetic anisotropy (VCMA) efficiency depending strongly on the Ir thickness and epitaxial strain effect. Furthermore, the spin reorientation has also been achieved with increased Ir thickness, and the magnitude and slope of VCMA behavior are dominated by the biaxial strain. We elucidate that the underlying mechanism is the electric-field-induced modifications of the spin-orbit coupling energies of the spin-polarized Ir-*d* orbitals. These findings not only reveal new approaches controlling 2D magnetism, but also pave the way of an alternative strategy for the design of nonvolatile and ultralow power spintronics and magnetic memory storage devices.

DOI: 10.1103/PhysRevB.107.075425

Magnetoelectric random access memory (MeRAM) has attracted substantial research interest as a promising memory architecture enabling ultralow power, highly scalable, nonvolatile and high-speed writing features [1–3]. In contrast to the current-driven magnetization switching scheme for the magnetic RAM (MRAM), the realization of MeRAM relies primarily on the voltage-controlled magnetic anisotropy (VCMA) mechanism which utilizes the electric field to efficiently manipulate spin orientations without Joule heating in magnetic tunnel junctions (MTJs) [4–7]. Unfortunately, to date there are still two impedimental factors in optimizing the performance of MeRAM device, namely, the perpendicular magnetic anisotropy (PMA) energy and VCMA coefficient. Typically, large PMA energy (>2 erg/cm^2) can assist in maintaining the information bit against thermodynamics fluctuations, while a greater VCMA coefficient ($>$ 1000 fJ/Vm) is required to achieve low switching energy (<1 fJ/bit), low write voltage (<1 V), and write error rate [8,9]. In the pursuit of better energy efficiency, various ferromagnetic-insulator interfaces with high tunnel magnetoresistance ratio have been explored such as the FeCo-based, Fe-based, and Heusler alloys heterostructures [10–12]. Moreover, the strategy with incorporation of heavy metal (HM) capping layers has been confirmed to push forward the advancement of VCMA behavior reaching few hundreds of fJ/Vm [13,14]. However, the PMA and VCMA coefficient of these traditional magnetic ultrathin films mainly originate from the complicated interfacial effect and electric field induced charge redistribution [15–17]. Therefore, the qualities of HM/FM and FM/insulators interfaces usually exhibit a decisive impact on their performances [16]. In view of the problem of traditional magnetic ultrathin films in fabricating high-quality samples limited by their dangling bond and high reactivity [18], searching alternative ferromagnetic materials would be essential to address the two major challenges for future MeRAM devices.

Meanwhile, the emergence of intrinsic two-dimensional (2D) magnetism achieved in experiments further expand the scope of ideal platforms for developing the desired MeRAM [19–21]. Instead of serving as a tunnel barrier by 2D dielectrics, these layered FM materials offer a new opportunity to substitute traditional magnetic thin films, and can be embedded as free or pinned layer to assemble MTJs [18,22–25]. Regarding the stacking quality, the covalently bonded 2D surfaces possess the ability to fully decouple from various junctions which in turn can facilitate the high-quality interfaces [26]. Currently, research works have focused on the electron transport properties of various MTJs consisting of 2D CrI_3, VSe_2, or Fe_3GeTe_2, and revealed their giant tunneling magnetoresistance (TMR) ratios ranging from 78% to 3600% [20,27–29]. On the other hand, given the unique crystal structures in ultimate thickness dimension, these 2D magnetic materials exhibit a weak electric screening effect and excellent flexibility which allow the electrical control. In fact, the voltage-controlled switching between antiferromagnetic (AFM) and FM states were demonstrated on diverse 2D magnetic materials [30–34]. These results clearly suggest that the choice of 2D FM layers to design MTJ architectures

*long.q.sun@gmail.com
†nick.kioussis@csun.edu

may be a feasible alternative towards higher PMA and VCMA efficiencies [35].

For a qualified 2D FM material used in the typical HM/FM/MgO junctions, several critical parameters are required: room-temperature ferromagnetism, suitable PMA energy, as well as compatible crystal lattices to MgO substrate. Therefore, Fe_2I_2 layer sharing analogous square lattice is one promising candidate FM material as its Curie temperature and strain-modified PMA reach 400 K and 1.65 erg/cm^2, respectively [19]. In terms of the capping layer, our prototype model will focus on the Ir with large SOC which was proved to be easily magnetized in experimental and theoretical works [8,36,37]. Notably, the modulation of PMA and electric field control of magnetism remains unexplored thus far in such kind of multilayers involving 2D magnetic layers.

In this work, we present systematic first-principles calculations for the Ir/Fe_2I_2/MgO heterostructures with the different Ir capping thickness. Both giant PMA and VCMA coefficient have been demonstrated in such multilayers to depend on the biaxial strain. Some of the systems show a reorientation of magnetic easy axis in responding to the change of Ir thickness. In addition, we find that the strain effect leads to distinct VCMA responses, which was verified by the change of SOC energy differences. The underlying atomic mechanism mainly lies on electric-field-induced shift of spin-polarized d_{z^2} and d_{yz} orbitals on the Ir layer. These findings pave the way for the development of highly efficient MTJs based on 2D FM material platform in the next-generation MeRAM devices.

Methodology. Our density functional theory (DFT) calculations were performed in conjunction with the projector augmented-wave (PAW) scheme, as implemented in the plane-wave basis Vienna *ab initio* simulation package (VASP) [38]. The generalized gradient approximation (GGA) parameterized by Perdew-Burke-Ernzerhof (PBE) was used for exchange and correlation contributions [39]. A kinetic energy cutoff of 500 eV was chosen for the plane-wave expansion of wave functions and the Monkhorst-Pack scheme of $32\times32\times1$ k-point sampling was adopted for the integration over the first Brillouin zone [40]. We applied a vacuum space of 15 Å along the z direction to separate the periodic films and the dipole corrections are also taken along [001]. All structures are fully optimized until the residual forces acting on the ions become less than 0.01 eV/Å. The convergence criteria for the energy of 10^{-6} eV was met. Spin-orbit coupling (SOC) is included in the calculations self-consistently. The DFT+U method was employed for the treatment of the strong correlated 3d elections on Fe orbitals ($U_{\text{eff}} = 2.5$ eV) [41]. The magnetocrystalline anisotropy (MCA) energy per unit interfacial area is defined as $E_{\text{MCA}} = (E_{[100]} - E_{[001]})/A$, where $E_{[100]}$ and $E_{[001]}$ represent the total energy with in-plane and out-of-plane magnetization, respectively, and A is the in-plane area of the unit cell.

Results and Discussion. Figure 1(a) shows the stacking configurations of MgO/Fe_2I_2/Ir(n) trilayer which are modeled by a slab supercell along the [001] direction. These considered multilayers consist of 2D Fe_2I_2 sandwiched by five MLs of rock-salt MgO and n-MLs fcc Ir (n = 1 ∼ 5). The Ir atoms located in Fe_2I_2/Ir interfaces are placed atop of the I atoms of Fe_2I_2 ML, and the MgO/Fe_2I_2 interfaces are designed by placing I atoms atop Mg atoms, which are

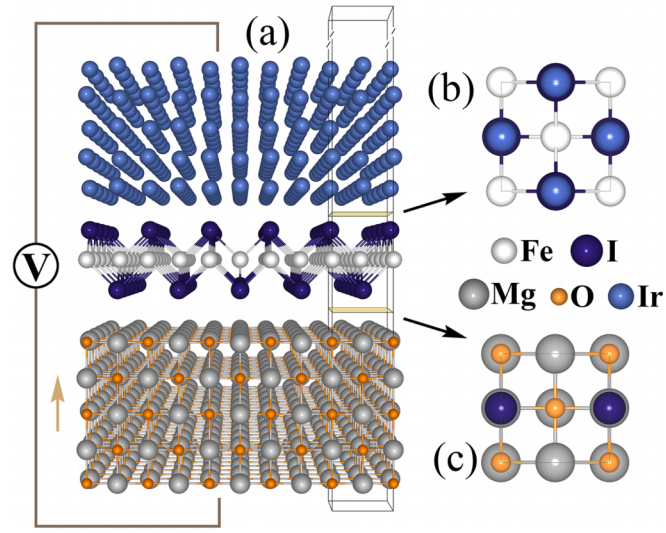

FIG. 1. (a) Schematic atomic structure of the MgO/Fe_2I_2/Ir heterostructure. The unit cell is denoted by the black parallelepiped. (b) and (c) show the stacking configurations of the Fe_2I_2/Ir and MgO/Fe_2I_2 interfaces, respectively.

the most stable crystalline structures [See Figs. 1(b) and 1(c)]. The lattice constants of Fe_2I_2 ML and initial bulk Ir are 3.810 and 3.839 Å, respectively, resulting in a negligible mismatch around 0.76%. It should be noticed that this mismatch ratio is much smaller that these of the FeCo-based junctions, and would promote the fabrication of high-quality interfaces in such heterostructures. Here, the in-plane lattice constants of the MgO/Fe_2I_2/Ir multilayer are set equal to that of bulk Ir (denoted as a_1) and 2D Fe_2I_2 (denoted as a_2), respectively, allowing for the study of the strain modulated effects. In fact, the optimized multilayers in Fig. 1(a) indeed represent atomically sharp and chemically clean interfaces without any disorder. The interlayer distances of Fe_2I_2/Ir(1) and MgO/Fe_2I_2 are 2.734 and 3.267 Å, respectively, under the lattice of a_1. When the lattice constant of the multilayer decreases to a_2, these interlayer distances become slightly enlarged to 2.790 and 3.298 Å, respectively. These stacking features also highlight the advantage of 2D materials which can largely decouple from the substrates and preserve their individual properties.

Having substantiated the stacking configurations of MgO/Fe_2I_2/Ir(n) heterostructures, in Fig. 2(a) we show the spin-resolved band structure of MgO/Fe_2I_2/Ir ($n = 1$) with lattice of a_1 as an example. It can be seen that the Fe_2I_2-resolved band dispersion is clearly identifiable compared with our previous results, where the majority-spin channel yields a large band gap and the minority spin shows linear band crossing [19]. The survived electronic structure of Fe_2I_2 ML mainly originates from the clean stacking interfaces. However, we find that the Fermi level shifts downward in energy below the crossing points. This finding suggests that interfacial charge transfer emerges in the interfaces of the multilayers. To gain more insight on the electronic migration, Fig. 2(b) depicts the charge difference (Δ_ρ) of the Fe_2I_2/Ir interface $\Delta_\rho = \rho_{\text{MgO/Fe}_2\text{I}_2\text{/Ir}} - \rho_{\text{MgO/Fe}_2\text{I}_2} - \rho_{\text{Ir}}$, where $\rho_{\text{MgO/Fe}_2\text{I}_2\text{/Ir}}$, $\rho_{\text{MgO/Fe}_2\text{I}_2}$ and ρ_{Ir} refer to the electron densities of the MgO/Fe_2I_2/Ir system, individual MgO/Fe_2I_2, and Ir layers, respectively. We

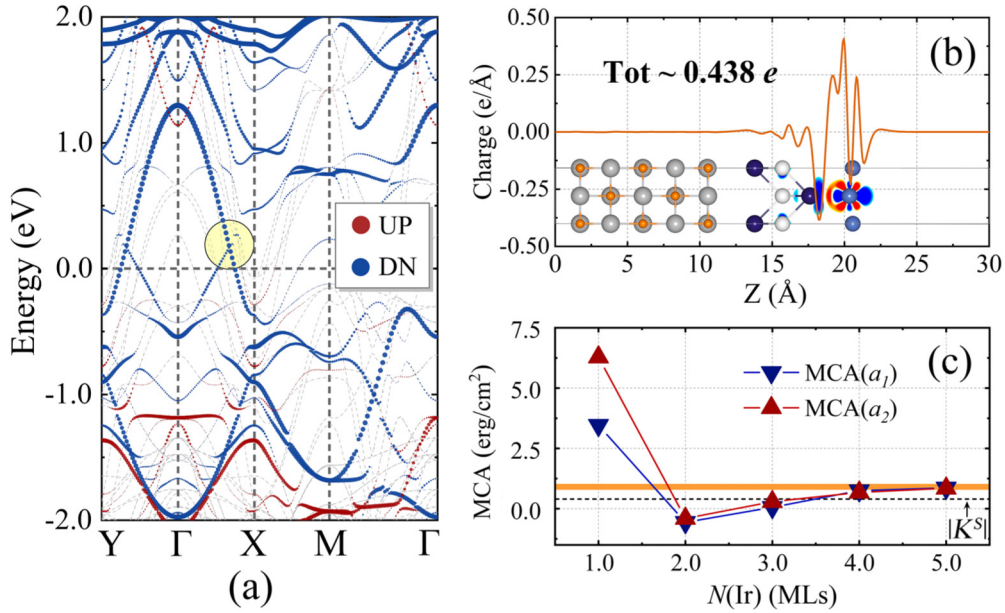

FIG. 2. (a) Atom- and spin-resolved band structures of the $MgO/Fe_2I_2/Ir(1)$ heterostructure based on the GGA+U method. (b) Plane-integrated electron density difference Δ_ρ for the $MgO/Fe_2I_2/Ir(1)$ heterostructure. The inset is the 3D isosurface of the electron density difference where the red and blue areas represent electron accumulation and depletion, respectively. (c) Variation of the MCA for the $MgO/Fe_2I_2/Ir$ as a function of Ir thickness (n) with different in-pane lattice constants of a_1=3.839 Å and a_2=3.810 Å, respectively. The horizontal dashed line denotes the shape anisotropy energy of K^s.

find that a notable electronic redistribution localizes at the Fe_2I_2/Ir interface with an accumulation of charges [red sphere in Fig. 2(b)] into the Ir layer originating from the interfacial I atoms [blue sphere in Fig. 2(b)]. The plane-integrated electron density also confirms that electrons are depleted on the Fe_2I_2 ML, giving a variation of 0.482 e^-. These findings are consistent with the mentioned shift of Fermi level for the $MgO/Fe_2I_2/Ir$ system.

The magnetic moments of Fe vary between 2.975 and 3.069 μ_B with different thickness of Ir layers, which is in agreement with the cases of 2D Fe_2I_2 (~2.973 μ_B). Besides, the emergence of local moments on the capped Ir are also confirmed in the Ir/Fe_2I_2 interfaces. The single Ir capping layer (n = 1) yields the largest magnetic moments of 1.224 and 0.986 μ_B per atom with the lattice constant of a_1 and a_2, respectively. These values of local moments are enhanced compared with the strain-induced moments on the free-standing Ir layer, which should originate from the proximity effect. In addition, we noticed that the compressive strain with the lattice constant of a_2 result in the reduction of magnetic moments on Ir, consistent with reported monotonic behavior of strain-driven magnetism of the free-standing Ir [42]. Therefore, the external strain and proximity effect show the synergistic effects to the induced magnetism of the Ir capping layers. For n $\geqslant$ 2 the local moments of interfacial Ir decrease dramatically and remain constant around 0.03 μ_B, which is one order of magnitude smaller than these of FeCo/TM interfaces [11,37]. On the other hand, the local moments of Ir layers away from the Fe_2I_2/Ir interfaces progressively decrease as the thickness increases, suggesting a thinner Ir capping layer would trigger more significant influences on the magnetic properties of $MgO/Fe_2I_2/Ir$ heterostructure.

Given the large spin-orbit-coupling (SOC) of Ir, the induced magnetized Ir caps would directly change the MCA of $MgO/Fe_2I_2/Ir$ multilayers. In Fig. 2(c) we show the calculated MCA for the multilayers with Ir-cap thickness n ranging from 1 to 5 MLs. For the $MgO/Fe_2I_2/Ir$ system with 1-ML Ir-cap, the MCA is found to be 3.461 and 6.285 erg/cm^2 with the lattice constant of a_1 and a_2, respectively, indicating a preference for out-of-plane magnetization. These MCAs are greatly enhanced by a factor of 4 ~ 8 compared with that of the pristine Fe_2I_2 ML. Besides, the strain strategy also exhibits critical effects on the modification of MCA in the capped system since a compressive strain of 0.76% yields a reduction of MCA by a factor of 1.8. Employing the Bruno expression, we have calculated the orbital moment anisotropy ($\Delta M_o = M_o^{001} - M_o^{100}$) of Ir under different lattice constants. Our results show that the ΔM_o changes from 0.162 to 0.106 μ_B as the multilayers undergo compressive strain, correlating with that of the MCA. The dashed line in Fig. 2(c) indicates the shape anisotropy energy $K^s = -\mu_0 M_s^2 t/2 = -0.402$ erg/cm^2 of the magnetic slab, which is about one order of magnitude smaller than its MCA.

Regarding the effect of Ir thickness (n) on the magnetic anisotropy, as shown in Fig. 2(c), the MCA declines dramatically below 0.86 erg/cm^2 with 2 to 5 MLs Ir caps (n = 2 ~ 5). Similar behaviors have been reported in the Ir capped FeCo thin films. However, unlike the variation trend of FeCo/Ir, the MCA for $MgO/Fe_2I_2/Ir$ system increases monotonically with thicker Ir capping layers, which eventually saturates at ~0.86 erg/cm^2. It is noteworthy that the corresponding multilayers with 2- or 3-MLs Ir cap exhibit negative magnetic anisotropy energies (below the dashed line) upon taking into account K^s, suggesting an out-of-plane to an in-plane magnetization reorientation. The underlying origin is the diminished magnetic

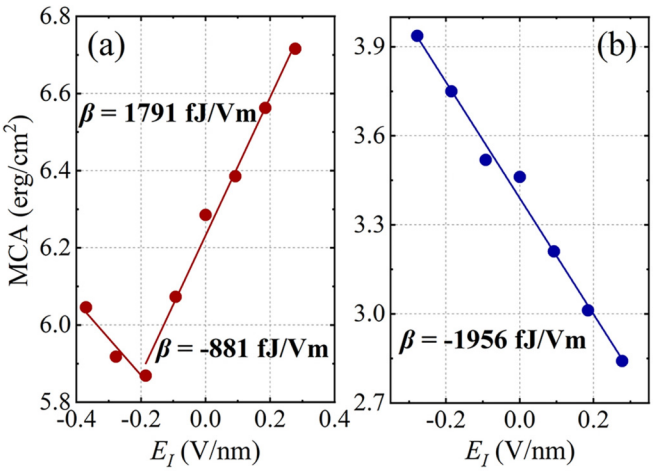

FIG. 3. The MCA of the $MgO/Fe_2I_2/Ir$ (n = 1) heterostructure as a function of electric field in MgO with lattice constant of (a) $a_1 = 3.839$ Å and (b) $a_2 = 3.810$ Å, respectively.

and orbital moments on the Ir, yielding a negative contribution to the MCA. When the Ir thickness reaches 5 MLs, the Fe atoms with ΔM_o around $0.032 \sim 0.043\ \mu_B$ dominantly contribute the MCA of the $MgO/Fe_2I_2/Ir$ system, leading to the MCA ranging from 0.847 to 0.861 erg/cm^2, similar to that of 2D Fe_2I_2 (orange stripe area). These findings demonstrate that the Ir cap layer can achieve the efficient modification of the magnetic properties of 2D Fe_2I_2, which is essential for future spintronic applications.

Next, to further probe the VCMA coefficient, an electric field is applied perpendicular to the $MgO/Fe_2I_2/Ir(1)$ heterostructure; as an example in view of that, 1ML Ir induces the highest PMA in the proposed multilayers. Figure 3 shows the variation of the MCA as a function of the electric field in MgO under different lattice constant. The VCMA coefficient (β) can be expressed in the linear regime as $\beta = \Delta E_{\rm MCA}/E_I$, where $\Delta E_{\rm MCA}$ is the electric-field-induced change of MCA, and E_I is the electric field in the insulator. We find that the epitaxial strain gives rise to a dramatic effect on the magnitude and sign of the VCMA efficiency. More specifically, the Ir-capped multilayer for the a_1 lattice constant shows an asymmetric V-shape field behavior with β values of 1791 (−881) fJ/Vm above (below) the critical field $E_I = -0.185$ V/nm. Here, the left part of the V-shape field behavior was confirmed by another point of MCA of 6.046 erg/cm^2 under the E-field of −0.370 V/nm. In contrast, the VCMA behavior for the a_2 lattice constant exhibits a linear response with the β value of −1956 fJ/Vm. These optimized values are comparable to the TM-based FeCo or Mn_3Ga junctions, which are about one order of magnitude higher than these of most experimentally reported values of FeCo-based MTJs with β in the range of $20 \sim 300$ fJ/Vm. Furthermore, we determined the influence of the Ir cap thickness on the VCMA coefficients, where the β values for the 1ML- and 3MLs Ir caps are summarized in Table I. We find that increasing the Ir overlayer thickness leads to the reduction in the VCMA coefficient, which shows asymmetric Λ-shape E-field behavior with a sign reversal. Here, the maximum $|\beta|$ for $MgO/Fe_2I_2/Ir(3)$ decreases to 593 and 701 fJ/Vm under a_1 and a_2 lattice constant, respectively. Therefore, these findings demonstrate that the 1ML-Ir-capped Fe_2I_2 multilayers could service as excellent material platforms for magnetoelectric spintronics, since the predicted giant VCMA coefficient values fulfill the requirement to achieve a switching bit energy below 1 fJ in the next generation of MeRAM. In addition, the feasibility of controlling the VCMA behavior via strain engineering was also demonstrated to design desired MeRAM devices.

TABLE I. The VCMA coefficient β (in fJ/Vm) of the $MgO/Fe_2I_2/Ir$ multilayers versus Ir cap thickness (in ML) under a_1=3.839 Å and a_2=3.810 Å.

β (fJ/Vm)	1ML-Ir		3ML-Ir	
a_1	−881	1791	593	−525
a_2	−1956		186	−701

In order to elucidate the microscopic origin of the giant VCMA efficiency in the $MgO/Fe_2I_2/Ir(1)$ multilayer, we have also calculated the atom-resolved SOC energy difference $\Delta E_{\rm SOC} = (E^{100}_{\rm SOC} - E^{001}_{\rm SOC})/2$ [43]. Here, $E^{100}_{\rm SOC}$ and $E^{001}_{\rm SOC}$ represent the SOC energies with in-plane and out-of-plane magnetization, given by

$$E_{\rm soc} = \frac{\hbar^2}{2m^2c^2}\left\langle \frac{1}{r}\frac{dV}{dr}\hat{L}\cdot\hat{\tilde{S}}\right\rangle, \tag{1}$$

where $V(r)$ is the spherical part of the effective potential within the PAW sphere. In view of the failure of perturbation theory due to the strong SOC of Ir ($\xi = 451$ meV), in Fig. 4(a) we display the E-field-induced changes of $\Delta E_{\rm SOC}$ and MCA for the $MgO/Fe_2I_2/Ir(1)$ with lattice constant of $a_1 = 3.839$ Å as an example, where $\delta E_{\rm SOC} = \Delta E_{\rm SOC}(E^1_I) - \Delta E_{\rm SOC}(E^2_I)$ and $\delta(\text{MCA}) = \text{MCA}(E^1_I) - \text{MCA}(E^2_I)$. It should be noted that the electric field-induced variation of $\delta E_{\rm SOC}$ has been found to correlate well to that of δ(MCA) sharing the similar asymmetric V-shape field behavior. Overall, the results reveal that Ir-resolved $\delta E_{\rm SOC}$ yields the dominant contribution to the total $\delta E_{\rm SOC}$ under the perpendicular electric field, indicating the giant VCMA coefficient mainly originates from the magnetized Ir. Similar conclusions have also been reported for 5d-TM modified magnetic thin films. However, our findings emphasize the feasibility to optimize 2D magnetism by stacking ultrathin 5d-TM layers with high-quality interfaces, giving rise to giant PMA and VCMA efficiency for MeRAMs.

The electric-field-driven modulation of MCA via the capped Ir can also be understood from the second-order perturbation theory, which assumes the MCA modifications are induced by changes of coupling strength between occupied and unoccupied d states through the orbital angular momentum operators $\hat{L}_z$ and $\hat{L}_x$, given by: [42,44]

$$\text{MCA} \approx \sum_{I,lmm'\sigma\sigma'} \sum_{o,u} \sigma\sigma'\xi^2_{Il}\frac{P^{Ilm\sigma}_u P^{Ilm'\sigma'}_o}{E^{\sigma}_u - E^{\sigma'}_o}\Delta L_{l,mm'}, \tag{2}$$

where

$$\Delta L_{l,mm'} = |\langle lm|\hat{L}_z|lm'\rangle|^2 - |\langle lm|\hat{L}_x|lm'\rangle|^2. \tag{3}$$

Here, $\hat{\xi}$ refers to the diagonal matrix containing the SOC strength; $\hat{L}_z(\hat{L}_x)$ denotes the z(x) component of the orbital

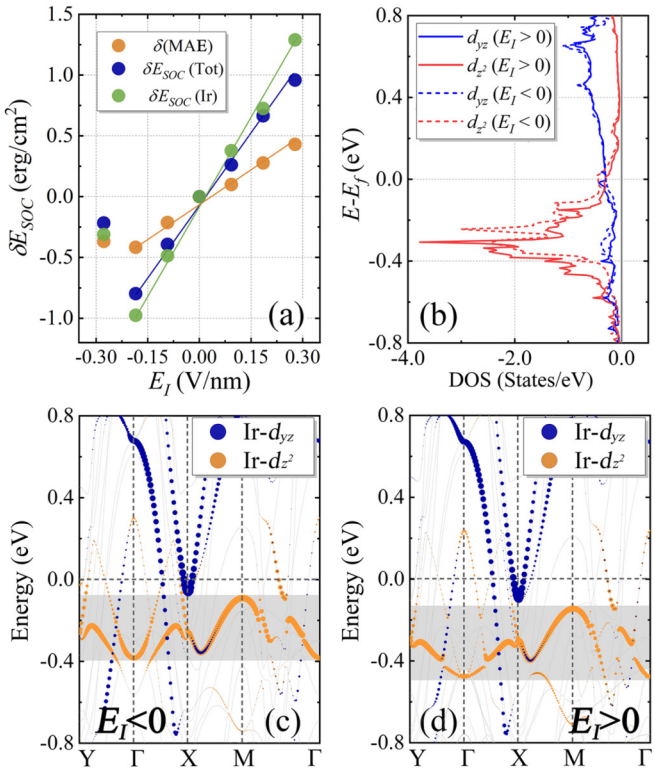

FIG. 4. (a) The electric-field-induced changes of SOC energies and MCA, i.e., $\delta E_{\rm SOC}$ and δ(MCA), relative to zero field ($E_I^2 = 0$) for the $MgO/Fe_2I_2/Ir(1)$ heterostructures. (b) The spin-projected density of states (DOS) of d_{yz} and d_{z^2} orbitals for Ir under E_I. Here, $E_I > 0$ ($E_I < 0$) denotes the applied E-field of $+0.278$ (-0.185) V/nm in MgO. Energy and k-resolved distributions of the minority-spin d-orbital of Ir under the external E-field of (c) -0.185 V/nm and (d) $+0.278$ V/nm, respectively.

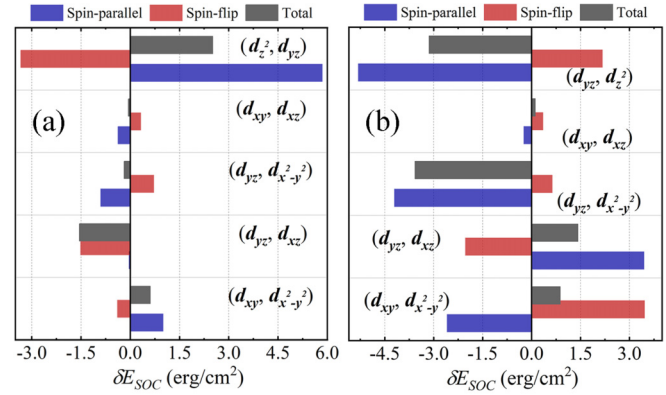

FIG. 5. The d orbital-projected contributions of Ir to the electric-field-induced change of SOC energy difference $\delta E_{\rm SOC}$ for the $MgO/Fe_2I_2/Ir(1)$ multilayer with lattice constant of (a) $a_1 = 3.839$ Å and (b) $a_2 = 3.810$ Å, respectively. Here, E_I^1 and E_I^2 are 0.278 (0.278) and $-0.185(-0.278)$ V/nm in the left (right) panel, respectively.

angular momentum operator; $P_n^{lm\sigma} = |\langle \Psi_n^\sigma || Ilm \rangle|^2$ is the Bloch wave amplitude projected on Ir atoms; orbital index lm; and spin index σ, $\Psi_n^\sigma(E_n^\sigma)$ is the one-electron occupied and unoccupied spin-polarized Bloch states (energies) of band index n and wave vector k (omitted for simplicity). Analysis of the orbital-resolved density of states (DOS) of the capped Ir atoms shows that the spin-minority occupied d_{z^2} and unoccupied d_{yz} are primarily responsible for the linear VCMA behavior under the E-field ranging from -0.185 to 0.278 V/nm. As shown in Fig. 4(b), the electric field has a larger effect on d_{z^2}-derived Ir projected DOS, which shift downward in energy as the E_I changes from negative to positive. In view of the unchanged d_{yz} states, this would cause a weaker of SOC coupling between d_{z^2} and d_{yz} through the $\hat{L}_x$ operator, which in turn reduces the negative term of $\langle d_{z^2}^\downarrow | \hat{L}_x | d_{yz}^\downarrow \rangle$ and eventually enhances the MCA.

In Figs. 4(c) and 4(d) we also show the minority-spin bands of the Ir-derived d_{z^2} and d_{yz} states with E-field of -0.185 and 0.278 V/nm, respectively. The results reveal that the SOC matrix element of $\langle d_{z^2}^\downarrow | \hat{L}_x | d_{yz}^\downarrow \rangle$ mainly yield negative contributions around Γ-X-M. Except for the rigid shift of the occupied d_{z^2} (gray area), it should be noted that the d_{z^2} states around Γ between -0.4 to 0 eV were eliminated when the E-field changes from -0.185 to 0.278 V/nm. Consequently, the vanished negative contributions around Γ further increases the MCA of the $MgO/Fe_2I_2/Ir(1)$ junction, yielding a positive VCMA coefficient. These findings in the electric-field-induced shift of the Ir-derived DOS are similar to other TM-capped traditional magnetic thin films, while the electric field mainly changes the atomic positions along the z direction and thus influences the charge accumulation and the out-of-plane d states.

In order to understand the sign reversal of the VCMA coefficient from 1791 to -1956 fJ/Vm with decreasing lattice constant shown in Figs. 3(a) and 3(b), we display the corresponding d orbital-projected contributions of Ir atoms to the electric-field-induced change of SOC energy difference in Fig. 5. For the larger lattice constant, Fig. 5(a) reveals that the spin parallel SOC matrix element $\langle d_{z^2}^\sigma | \hat{L}_x | d_{yz}^\sigma \rangle$ yields the dominant contribution to the increase of $\delta E_{\rm SOC}$. This finding indicates that the negative value of the SOC between $d_{z^2}^\sigma$ and d_{yz}^σ through in-plane orbital angular-momentum operator ($\hat{L}_x$) becomes weaker when the E_I changes from -0.185 to 0.278 V/nm, resulting in a positive VCMA coefficient. Furthermore, for the smaller lattice constant, the monotonic decrease of MCA originates primarily from the spin-parallel SOC of the $\langle d_{z^2}^\sigma | \hat{L}_x | d_{yz}^\sigma \rangle$ and $\langle d_{yz}^\sigma | \hat{L}_x | d_{x^2-y^2}^\sigma \rangle$ matrix elements shown in Fig. 5(b). In contrast to the results for $a_1 =$ 3.839 Å, the electric-field-induced changes of $\langle d_{z^2}^\sigma | \hat{L}_x | d_{yz}^\sigma \rangle$ and $\langle d_{yz}^\sigma | \hat{L}_x | d_{x^2-y^2}^\sigma \rangle$ are negative, indicating these spin parallel SOC terms become more negative as the electric field increases leading in turn to the VCMA coefficient sign reversal.

Conclusion. In summary, we propose a new general approach to assemble high-efficient voltage-controlled MTJ based on the 2D magnetic Fe_2I_2 layer, instead of the traditional ferromagnetic thin films, with Ir capping layers. Employing *ab initio* electronic structure calculations, the key parameters, such as the Ir capping layer thickness and epitaxial strain, have been investigated to optimize the MCA and VCMA coefficient for the $MgO/Fe_2I_2/Ir$ stacking architectures. We find that the MCA magnitude and spin orientation as well as the VCMA coefficients exhibit strong dependence

on Ir thickness. Notably, reducing the Ir thickness down to monolayer can significantly enhance the MCA of the multilayers, and spin reorientation has been achieved in the $MgO/Fe_2I_2/Ir(2/3)$ heterostructure. These primarily arise from the change of magnetic and orbital moments in Ir layers, which are dominated by the biaxial strain and proximity effect. In addition, we predict extremely high VCMA coefficients with a sign reversal behavior for the $MgO/Fe_2I_2/Ir(1)$ system exceeding the required 1000 fJ/Vm threshold, where the VCMA magnitude and slope depend dramatically on biaxial strain. Our results reveal that the underlying origin of the VCMA behavior lies on the electric-field-induced modifications of SOC couplings between the Ir-$d^{\sigma}_{z^2}$, -d^{σ}_{yz}, and -$d^{\sigma}_{x^2-y^2}$ orbitals through the $\hat{L}_x$ operator. These findings highlight the feasibility to fabricate the Ir-modified 2D magnetism for controllable magnetoelectronic nonvolatile devices.

Acknowledgments. This research was supported by the National Natural Science Foundation of China (Grant No. 12104257); the Shandong Provincial Natural Science Foundation, China (Grant No. ZR2021QA086), and the Doctoral Research Fund of Shandong Jianzhu University (Grant No. X21056Z). The work at CSUN is supported by NSF ERC-Translational Applications of Nanoscale Multiferroic Systems (TANMS), Grant No. 1160504, and by NSF-Partnership in Research and Education in Materials (PREM) Grant No. DMR-1205734.

[1] N. Spaldin and R. Ramesh, Advances in magnetoelectric multiferroics, Nat. Mater. **18**, 203 (2019).

[2] Y. Shiota, T. Nozaki, F. Bonell, S. Murakami, T. Shinjo, and Y. Suzuki, Induction of coherent magnetization switching in a few atomic layers of FeCo using voltage pulses, Nat. Mater. **11**, 39 (2012).

[3] W. G. Wang, M. Li, S. Hageman, and C. L. Chien, Electric-field-assisted switching in magnetic tunnel junctions, Nat. Mater. **11**, 64 (2012).

[4] T. Maruyama, Y. Shiota, T. Nozaki, K. Ohta, N. Toda, M. Mizuguchi, A. A. Tulapurkar, T. Shinjo, M. Shiraishi, S. Mizukami, Y. Ando, and Y. Suzuki, Large voltage-induced magnetic anisotropy change in a few atomic layers of iron, Nat. Nanotechnol. **4**, 158 (2009).

[5] M. Weisheit, S. Fahler, A. Marty, Y. Souche, C. Poinsignon, and D. Givord, Electric field-induced modification of magnetism in thin-film ferromagnets, Science **315**, 349 (2007).

[6] C. Grezes, F. Ebrahimi, J. G. Alzate, X. Cai, J. A. Katine, J. Langer, B. Ocker, P. K. Amiri, and K. L. Wang, Ultra-low switching energy and scaling in electric-field-controlled nanoscale magnetic tunnel junctions with high resistance-area product, Appl. Phys. Lett. **108**, 012403 (2016).

[7] D. Zhang, M. Bapna, W. Jiang, D. Sousa, Y.-C. Liao, Z. Zhao, Y. Lv, P. Sahu, D. Lyu, A. Naeemi, T. Low, S. A. Majetich, and J.-P. Wang, Bipolar electric-field switching of perpendicular magnetic tunnel junctions through voltage-controlled exchange coupling, Nano Lett. **22**, 622 (2022).

[8] Q. L. Sun, S. Kwon, M. Stamenova, S. Sanvito, and N. Kioussis, Electric field modulation of magnetism in ferrimagnetic heusler heterostructures, Phys. Rev. B **101**, 134419 (2020).

[9] K. L. Wang, H. Lee, and P. Khalili Amiri, Magnetoelectric random access memory-based circuit design by using voltage-controlled magnetic anisotropy in magnetic tunnel junctions, IEEE Trans. Nanotechnol. **14**, 992 (2015).

[10] S. Yuasa, T. Nagahama, A. Fukushima, Y. Suzuki, and K. Ando, Giant room-temperature magnetoresistance in single-crystal Fe/MgO/Fe magnetic tunnel junctions, Nat. Mater. **3**, 868 (2004).

[11] W. Z. Chen, L. N. Jiang, Z. R. Yan, Y. Zhu, C. H. Wan, and X. F. Han, Controlled magnetic anisotropy in a Cr/Fe/MgO junction with an ultrathin Fe layer: First-principles investigation, Phys. Rev. B **101**, 144434 (2020).

[12] A. Qurat, D. Odkhuu, S. H. Rhim, and S. C. Hong, Enhanced voltage-controlled magnetic anisotropy via magnetoelasticity in FePt/MgO(001), Phys. Rev. B **101**, 214436 (2020).

[13] G. H. Zheng and N. Kioussis, Ta cap-induced stabilization of interfacial ferromagnetism and enhanced magnetoelectricity in ultrathin FeRh films, J. Magn. Magn. Mater. **539**, 168414 (2021).

[14] A. P. Chen and Y. P. Feng, Modulating multiferroic control of magnetocrystalline anisotropy using 5d transition metal capping layers, ACS Appl. Mater. Interfaces **12**, 25383 (2020).

[15] Y. C. Wu, W. Kim, S. Van Beek, S. Couet, R. Carpenter, S. Rao, S. Kundu, J. Van Houdt, G. Groeseneken, D. Crotti, and G. S. Kar, Impact of ambient temperature on the switching of voltage-controlled perpendicular magnetic tunnel junction, Appl. Phys. Lett. **118**, 122404 (2021).

[16] B. F. Vermeulen, J. Swerts, S. Couet, M. Popovici, I. P. Radu, J. Van de Vondel, K. Temst, G. Groeseneken, and K. Martens, Electronic voltage control of magnetic anisotropy at room temperature in high-κ $SrTiO_3$/Co/Pt trilayer, Phys. Rev. Mater. **4**, 114415 (2020).

[17] C. A. F. Vaz, J. Hoffman, A.-B. Posadas, and C. H. Ahn, Magnetic anisotropy modulation of magnetite in $Fe_3O_4/BaTiO_3$ epitaxial structures, Appl. Phys. Lett. **94**, 022504 (2009).

[18] X. L. Sui, T. Hu, J. F. Wang, B. L. Gu, W. H. Duan, and M. S. Miao, Voltage-controllable colossal magnetocrystalline anisotropy in single-layer transition metal dichalcogenides, Phys. Rev. B **96**, 041410(R) (2017).

[19] Q. L. Sun, Y. D. Ma, and N. Kioussis, Two-dimensional Dirac spin-gapless semiconductors with tunable perpendicular magnetic anisotropy and a robust quantum anomalous Hall effect, Mater. Horiz. **7**, 2071 (2020).

[20] L. S. Zhang, J. Zhou, H. Li, L. Shen, and Y. P. Feng, Recent progress and challenges in magnetic tunnel junctions with 2D materials for spintronic applications, Appl. Phys. Rev. **8**, 021308 (2021).

[21] B. Huang, G. Clark, E. Navarro-Moratalla, D. R. Klein, R. Cheng, K. L. Seyler, D. Zhong, E. Schmidgall, M. A. McGuire, D. H. Cobden *et al.*, Layer-dependent ferromagnetism in a van der Waals crystal down to the monolayer limit, Nature (London) **546**, 270 (2017).

[22] M. Piquemal-Banci, R. Galceran, F. Godel, S. Caneva, M. B. Martin, R. S. Weatherup, P. R. Kidambi, K. Bouzehouane, S. Xavier, A. Anane, F. Petroff, A. Fert, S. M. Dubois, J. C.

Charlier, J. Robertson, S. Hofmann, B. Dlubak, and P. Seneor, Insulator-to-metallic spin-filtering in 2D-magnetic tunnel junctions based on hexagonal Boron Nitride, ACS Nano **12**, 4712 (2018).

[23] E. C. Ahn, 2D materials for spintronic devices, npj 2D Mater. Appl. **4**, 17 (2020).

[24] P. Huang, P. Zhang, S. Xu, H. Wang, X. Zhang, and H. Zhang, Recent advances in two-dimensional ferromagnetism: materials synthesis, physical properties and device applications, Nanoscale **12**, 2309 (2020).

[25] Y. Liu and Q. Shao, Two-dimensional materials for energy-efficient spin-orbit torque devices, ACS Nano **14**, 9389 (2020).

[26] C. Gong and X. Zhang, Two-dimensional magnetic crystals and emergent heterostructure devices, Science **363**, eaav4450 (2019).

[27] Z. Z. Lin, and X. Chen, Ultrathin scattering spin filter and magnetic tunnel junction implemented by ferromagnetic 2D van der Waals material, Adv. Electron. Mater. **6**, 1900968 (2020).

[28] Z. Wang, D. Sapkota, T. Taniguchi, K. Watanabe, D. Mandrus, and A. F. Morpurgo, Tunneling spin valves based on Fe_3GeTe_2/hBN/Fe_3GeTe_2 van der Waals heterostructures, Nano Lett. **18**, 4303 (2018).

[29] J. Chu, Y. Wang, X. Wang, K. Hu, G. Rao, C. Gong, C. Wu, H. Hong, X. Wang, K. Liu, C. Gao, and J. Xiong, 2D polarized materials: Ferromagnetic, ferrovalley, ferroelectric materials, and related heterostructures, Adv. Mater. **33**, 2004469 (2021).

[30] X. Jiang, Q. X. Liu, J. P. Xing, N. S. Liu, Y. Guo, Z. F. Liu, and J. J. Zhao, Recent progress on 2D magnets: Fundamental mechanism, structural design and modification, Appl. Phys. Rev. **8**, 031305 (2021).

[31] C. Huang, J. Zhou, H. Sun, F. Wu, Y. Hou, and E. Kan, Toward room-temperature electrical control of magnetic order in multiferroic van der Waals materials, Nano Lett. **22**, 5191 (2022).

[32] M. Xu, C. Huang, Y. Li, S. Liu, X. Zhong, P. Jena, E. Kan, and Y. Wang, Electrical Control of Magnetic Phase Transition in a Type-I Multiferroic Double-Metal Trihalide Monolayer, Phys. Rev. Lett. **124**, 067602 (2020).

[33] B. Huang, G. Clark, D. R. Klein, D. MacNeill, E. Navarro-Moratalla, K. L. Seyler, N. Wilson, M. A. McGuire, D. H. Cobden, D. Xiao *et al.*, Electrical control of 2D magnetism in bilayer CrI_3, Nat. Nanotechnol. **13**, 544 (2018).

[34] H. Wang, N. Mao, C. Niu, S. Shen, M.-H. Whangbo, B. Huang, and Y. Dai, Ferromagnetic dual topological insulator in a two-dimensional honeycomb lattice, Mater. Horiz. **7**, 2431 (2020).

[35] M. Alsubaie, C. Tang, D. Wijethunge, D. Qi, and A. Du, First-principles study of the enhanced magnetic anisotropy and transition temperature in a $CrSe_2$ monolayer via hydrogenation, ACS Appl. Electron. Mater. **4**, 3240 (2022).

[36] Y. Kato, H. Yoda, Y. Saito, S. Oikawa, K. Fujii, M. Yoshiki, K. Koi, H. Sugiyama, M. Ishikawa, T. Inokuchi, N. Shimomura, M. Shimizu, S. Shirotori, B. Altansargai, Y. Ohsawa, K. Ikegami, A. Tiwari, and A. Kurobe, Giant voltage-controlled magnetic anisotropy effect in a crystallographically strained CoFe System, Appl. Phys. Express **11**, 053007 (2018).

[37] S. Kwon, P. V. Ong, Q. L. Sun, F. Mahfouzi, X. Li, K. L. Wang, Y. Kato, H. Yoda, P. K. Amiri, and N. Kioussis, Colossal electric field control of magnetic anisotropy at ferromagnetic interfaces induced by iridium overlayer, Phys. Rev. B **99**, 064434 (2019).

[38] G. Kresse and J. Furthmüller, Efficient iterative schemes for ab initio total-energy calculations using a plane-wave basis set, Phys. Rev. B **54**, 11169 (1996).

[39] J. P. Perdew, K. Burke, and M. Ernzerhof, Generalized Gradient Approximation Made Simple, Phys. Rev. Lett. **77**, 3865 (1996).

[40] H. J. Monkhorst and J. D. Pack, Special points for Brillouin-zone integrations, Phys. Rev. B **13**, 5188 (1976).

[41] V. I. Anisimov, F. Aryasetiawan, and A. I. Lichtenstein, First-principles calculations of the electronic structure and spectra of strongly correlated systems: The LDA+U method, J. Phys.: Condens. Matter **9**, 767 (1997).

[42] S. Kwon, Q. Sun, F. Mahfouzi, K. L. Wang, P. K. Amiri, and N. Kioussis, Voltage-Controlled Magnetic Anisotropy in Heterostructures with Atomically Thin Heavy Metals, Phys. Rev. Appl. **12**, 044075 (2019).

[43] K. Bairagi, A. Bellec, V. Repain, C. Chacon, Y. Girard, Y. Garreau, J. Lagoute, S. Rousset, R. Breitwieser, Yu-Cheng Hu, Yen Cheng Chao, W. W. Pai, D. Li, A. Smogunov, and C. Barreteau, Tuning the Magnetic Anisotropy at a Molecule-Metal Interface, Phys. Rev. Lett. **114**, 247203 (2015).

[44] F. Gimbert and L. Calmels, First-principles investigation of the magnetic anisotropy and magnetic properties of Co/Ni(111) superlattices, Phys. Rev. B **86**, 184407 (2012).